IEEE Access
Multidisciplinary | Rapid Review | Open Access Journal

Received 11 March 2023, accepted 6 April 2023, date of publication 12 April 2023, date of current version 17 April 2023.

Digital Object Identifier 10.1109/ACCESS.2023.3266657

RESEARCH ARTICLE

Research on the Automatically Independent Controlling Algorithm of the Grid-Connected PV Inverter Jointly Considering Dynamic Load Features and Active LVRT Capability

WANG JINPENG[1], ZHANG BO[1], YAO QINXUE[1], JEREMY-GILLBANKS[2], AND ZHAO XIN[1], (Member, IEEE)

[1]School of Information Science and Engineering, Dalian Polytechnic University, Dalian, Liaoning 116039, China
[2]School of Electronic, Electrical and Computer Engineering, The University of Western Australia, Perth, WA 6009, Australia

Corresponding author: Wang Jinpeng (wangjp@dlpu.edu.cn)

This work was supported in part by the National Natural Science Foundation of China under Grant 61402069; the Fundamental Research Funds for the Central Universities under Grant 3132016317; in part by the 2017 and 2020 Projects of the Natural Science Foundation of Liaoning Province under Grant 20170540059 and Grant J2020018; in part by the General Project of Liaoning Education Department, in 2016, under Grant 2016J205; and in part by the General Project of the National Social Science Fund under Grant 2019AG00482.

ABSTRACT Due to environmental and energy policies in recent years, some countries will install many PV generations into power systems in the future. Under this condition, it is worrisome that the disconnection of the PV occurs because of a voltage drop triggered via a system fault, which impacts the stability of the PV(photovoltaic).A technique of FRT (Fault Ride Through) is an expected solution for PVs. However, just the FRT requirements for PVs do not inevitably increase the stability of the power system. Solving the problem of the instability of the inverter control in a grid-connected PV needs reasonable consideration. This paper proposed an automatically independent controlling algorithm of the PV inverter considering dynamic load features and Active LVRT (low voltage ride through) capability to increase the robustness and performance of the grid-connected PV system, and both simulation and experimental results showed that the condition of a range from an IM rate = 20[%] to an IM rate=40[%] could best meet the requirements for the PV outputting recovery and the average tracking error of the input current reduced by nearly 10%. Also, the average output current tracking error was reduced by about 4%. This shows that the tracking performance has significantly improved.

INDEX TERMS PV inverter, fault ride through, grid-connected, PV system.

I. INTRODUCTION

In recent years, PV generation has been growing fast. It is necessary to address the negative effect of the high permeability PV on the grid [1] for improvement. Stability is a vital problem in a PV system [2]. With the quick increase in solar irradiance, the PV generation may cause the voltage to exceed, which is overload [3], and other problems will arise when the PV system steps into an island model once the grid fails [4]. An intelligent PV inverter can transform the PV generation from a stability hazard to a stability asset using the controlling function [5], [6]. For several decades, scientists [7], [8], [9], [10] have studied and discussed updating the grid specifications related to the PV inverters to include the above capabilities, which some grid regulars have implemented. Nevertheless, it is difficult to control the PV inverter while adjusting the set values of the active and reactive power to realize the initial support of grid voltage [11], [12], [13], [14], [15].

The control method of the grid-connected photovoltaic inverter itself is a complex control problem because it usually requires cascade control loops. The reason is that

The associate editor coordinating the review of this manuscript and approving it for publication was Tariq Masood.

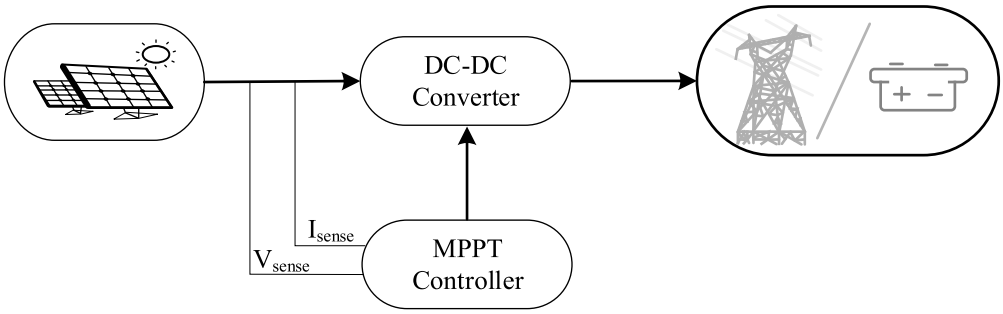

FIGURE 1. Model of the MPPT system.

grid-connected photovoltaics usually connect to the power grid through a two-stage converter which means a DC/DC boost converter after the DC/AC inverter stage [16], [17], [18].The first stage implements maximum power point tracking control (MPPT, as shown in Figure 1) and improves the photovoltaic voltage to meet the DC bus voltage requirements.

Meanwhile, the DC/AC inverter stage regulates the bus voltage and ensures the stability of the photovoltaic grid connection [19], [20]. The converter containing an impedance network [21] is called an impedance source inverter or Z-Source Inverter (ZSI) [22], [23], [24], [25], [26]. This topology can eliminate DC-DC converters or the need for transformers on the AC side, thus potentially reducing the total cost of converters and improving their efficiency [27].

Some researchers [28], [29], [30], [31] consider that a lot of countries will install some PVs into their grid power systems in the future because of energy and environmental policies [32]. For example, the ''TWO Carbon'' goals of 'carbon peak' as well as 'carbon neutral' firstly advocated by China on May 26, 2021 [33].

Many PVs installed into the grid power system will lead to a great worry about disconnections in the PV generations owing to a specific system fault [34], which could affect the PV system's both voltage stability and transient stability [35]. Some latest reports [36] proved that FRT demands in PVs impact positively on the stable ability of the PV system, which can reconnect to the grid and recover the output in the grid based on the FRT technique even after disconnection of the PVs from a power system.

Nevertheless, it is yet not sure how an FRT requirement for a PV impacts the PV system if thinking about some dynamic load features, just like the induction motor load [40]. Consequently, this research presented an automatically independent control algorithm of the PV inverter jointly considering dynamic load features and an active LVRT capability not only to explore and prove a mechanism of the FRT effects on the PV system, but also to improve the performance and robustness of the grid-connected PV system mentioned before.

Consequently, this research proposed the autonomous model predictive control (AMPC) scheme for intelligent PV inverters to achieve smooth switching between LVRT and MPPT modes under random grid conditions.

Firstly, this research analyzed dynamic load instances and the transient state concerning fault cases and provided the best meeting requirements for the PV outputting recovery and the average tracking error of the input current using simulation; In addition, this paper proposed a model of the Automatically Independent Controlling Algorithm of the grid-connected PV inverter jointly considering dynamic load features and active LVRT capability; Moreover, the report did the simulation and an experiment to verify the performance of the presented method.

The paper is structured as follows: Section I introduces the background of the article; Section II illustrates the stability of the PV system. Besides, this part analyses the transient state concerning fault cases as well as dynamic load cases; section III gives the proposed model of an automatically independent controlling algorithm of the PV inverter; Section IV shows and analyses the simulation and experimental results. The last section V concludes the whole paper.

II. POWER SYSTEM STABILITY

A. TRANSIENT STABILITY

Just like a short circuit over a transmitting, a large-disturbance rotor angle or transient stability depends on the ability of the PV system to keep the synchronism when a serious disturbance happens. The rotor angle of a generator is as the following swing equation [33] shows:

$$M\frac{\mathrm{d}^2\delta}{dt^2} = P_m - P_e \tag{1}$$

In expression (1), M symbolizes inertia constant, δ means the rotor angle, P_m represents the mechanical input, and P_e is an electrical output.

Therefore, on the one hand, a generator will decelerate once P_{PV} increases, and P_L is a fixed value; on the other hand, while P_L is a fixed value and P_{PV} increases before a fault or after clearing the wrong action, the generator will accelerate.

B. STABILITY OF THE VOLTAGE

Voltage stability is the ability of the PV circuit to keep the voltages on all buses of the system affected by a specific

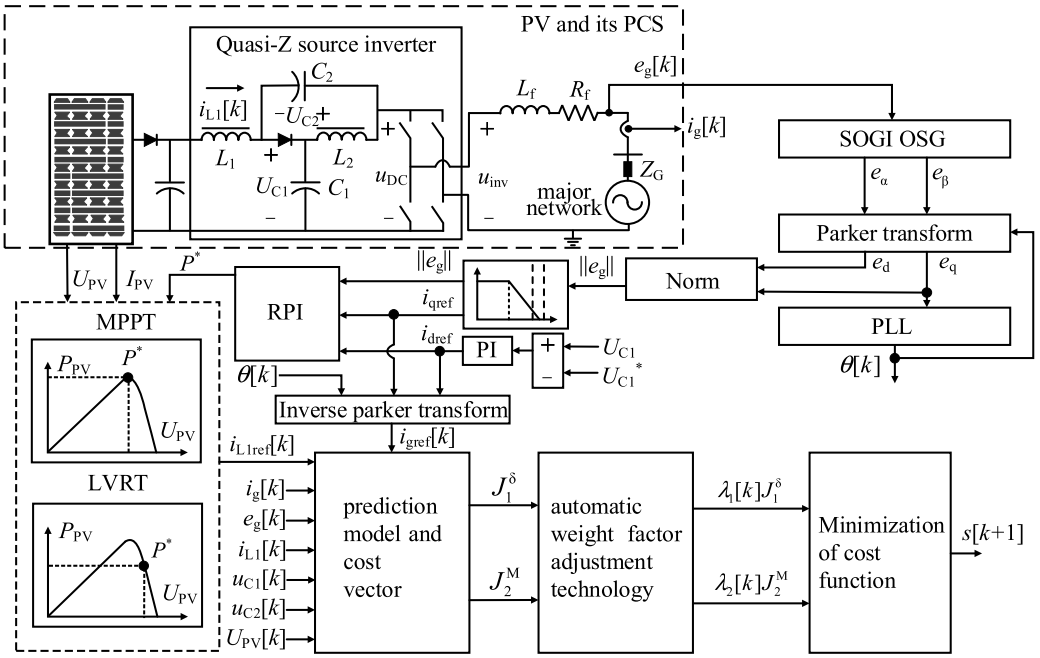

FIGURE 2. The proposed system model.

disturbance under the condition of a given initial state. For instance, an induction motor load with a constant power feature can strongly impact this voltage instability. Consequently, it is possible enough that the electrical power output of the PV system also can affect the voltage stability.

III. PROPOSED SYSTEM MODEL AND ITS CONTROL PROCESS

A. PROPOSED SYSTEM MODEL

Figure 2 gives the proposed System model and its control process, and it is a new photovoltaic system based on the QZSI (Quasi impedance Source Inverter) with a voltage fed. In this research, the PI controller prevents transient response from worse performance when control commends saturate.

The model shown in Figure 2 has five main modules, including a Quasi-Z source inverter, prediction model and cost vector, automatic weight factor adjustment technology, and minimization of cost function. Two converters, namely Parker transformer and inverse Parker one.

The system operates an auto-tuning through the module of 'automatic weight factor adjustment technology' in this figure. The automatic adjustment of weighting factors only explains one objective without losing generality. Consider the threshold of acceptable target error. In other words, if QZSI can keep the standardized control target less than its reference value, it is considered that the system has tracked the target, and no need for remedial measures.

This model operates in two modes:

1. when the grid voltage is within 90%-110% of its rated value, the system works in its normal mode and applies the predictive MPPT technology to ensure that the PV can obtain the MPP(Maximum Power Point).

2. when the grid voltage dip exceeds 10% of its rated value, the model operates its LVRT mode and transfers the QZSI to the supporting grid as an auxiliary service of the photovoltaic inverter from the MPPT operation.

B. CONTROL PROCESS

Supposing the whole switching period is T, the usual state time is T_1, and the fault time is T_0.

Moreover, by applying a volt-second balance on inductances L_1 and L_2 and making an average voltage in a switching period equal to zero, the following formulas can give the voltage of capacitors C_1, C_2, and the DC port:

$$U_{C1} = \frac{(1-D) \times U_{PV}}{1-2D} \tag{2}$$

$$U_{C2} = \frac{D \times U_{PV}}{1-2D} \tag{3}$$

$$U_{DC} = \frac{U_{PV}}{1-2D} \tag{4}$$

In the equations (2,3,4), D=T0/T is the duty cycle. The duty cycle D, the proportion of the power-on time to the total time in a pulse cycle, is responsible for the ratio of load or circuit opening time to load or circuit closing time in a PV system.

In general, the control of the QZSI requires simultaneous control of multiple system components, such as U_{C1}, i_{L1}, and i_g, but the cost function of the proposed algorithm does not include U_{C1}.

In addition, the system uses a PI (Proportional and Integral) controller to regulate U_{C1}, generates $i_{d,ref}$ using a proper control strategy, and finally achieves the QZSI by connecting to the grid through an MPC (Model Predictive Control).

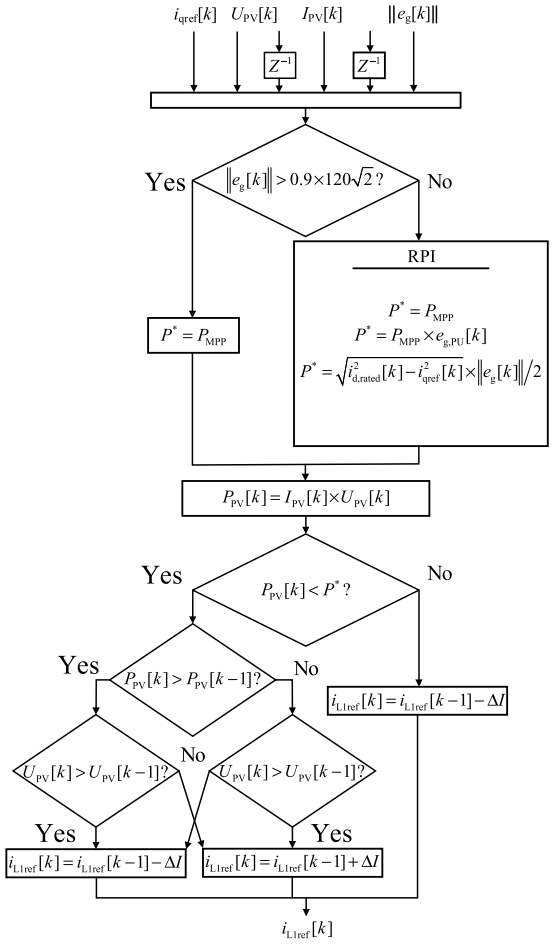

FIGURE 3. Control process of the proposed model.

Figure 3 illustrates the control process of the proposed model. The control strategy model has five judging modules and five functional modules. This process can generate PV reference current or average reference inputting inductance current i_{L1} for MPPT operation.

The controller will produce the referencing current i_{dref} of active components and put it into the grid through QZSI. Under this mode, the system maintains the reactive power component i_{qref} as zero and makes the QZSI work at the unity power factor. And then, the system will convert i_{dref} and i_{qref} to the phase current i_{gref} and feed it back to the MPC cost function together with $i_{L1,ref}$ from the MPPT algorithm. The following part explains this controlling process in detail:

By utilizing the VCR (Voltage Current Relationship) and applying the forward Euler method on the current equation of an active inductor, expression (5) below gives the discretization model of i_{L1}:

$$i_{L1}[k+1] = i_{L1}[k] + T_S (L_1)^{-1} (U_{PV}[k] - \delta U_{C1}[k] + (1-\delta) U_{C2}[k]) \delta \in [0, 1] \quad (5)$$

In formula (5), $i_{L1}[k+1]$ is the predicted inductance current, and δ symbolizes a non-crossing index. Accordingly, the sub-cost vector of these two elements is as follows:

$$\boldsymbol{J}_1^{\delta} = \left| i_{L1}[k+1] - i_{L1,ref}[k] \times \frac{1}{i_{L1,RMS}[k]} \right| \quad (6)$$

In equation (6), $i_{L1,RMS}[k]$ is used to normalize costs. As shown in the expressions below, utilizing the KVL equation (7) of the grid side can discretize i_g in formula (8) using the Euler forward method:

$$u_{inv} = R i_g + L \frac{di_g}{dt} + e_g \quad (7)$$

$$i_g[k+1] = i_g[k] (1 - \frac{R}{L} T_S + \frac{T_S}{L} (u_{inv}[k] - e_g[k]) \quad (8)$$

$$u_{inv}[k] = M \times (U_{C1}[k] + U_{C2}[k]), M \in [-1, 0, 1] \quad (9)$$

Since the output current prediction depends on the output voltage level M, the cost vector of the output current is equation (10):

$$\boldsymbol{J}_1^{\delta} = \left| i_g[k+1] - i_{gref}[k] \right| \times \frac{1}{i_{g,RMS}[k]} \quad (10)$$

In formula (10), $i_{g,RMS}[k]$ is a rolling RMS (Root Mean Square) measurement. The cost vector depends on its next state prediction, which depends on M. Finally, the two states are in a state of the couple because the ride-through limits the output voltage level. Although the real independent variable is the switching state s, the definitions of the cost vectors $\boldsymbol{J}_1^{\delta}$ and $\boldsymbol{J}_2^{M}$ are not according to s, but δ And M. Consequently, this method can reduce iterative computation using a less vector length. Finally, the system will summarize the sub-cost vector and its corresponding weight factor into the cost function vector.

$$\begin{cases} s_{opt} = \arg \text{minimize}(\boldsymbol{J}[s]) \\ \boldsymbol{J}[s] = \lambda_1 \boldsymbol{J}_1^{\delta} + \lambda_2 \boldsymbol{J}_2^{M} \end{cases} \quad (11)$$

In equation (11), s_{opt} represents the gate signal associated with each switch in state M.

IV. DYNAMIC LOAD AND SIMULATION

A. PV OUTPUT FEATURES

Using PCSs (Power Conditioning Systems) connects PVs to the power system, which can convert to AC power from DC power of PV. Figure 4 below models the electrical power outputting features in the article. Controlling not to be more than the limited value could protect PCSs from an over-current. As found in this Figure, the electrical power output of the PV tends to be constant in the usual condition, except the outputting current of the PV which tends to be stable once the voltage of the connecting point is small. Also, the power system will disconnect the PV at that node when the voltage decreases to be less than the lower limit.

B. REQUIREMENTS OF THE FRT

When a severe disturbance happens in the PV systems, the system disconnects from the PVs because of the faults. It is of great worry that the stability of the voltage of the PV system

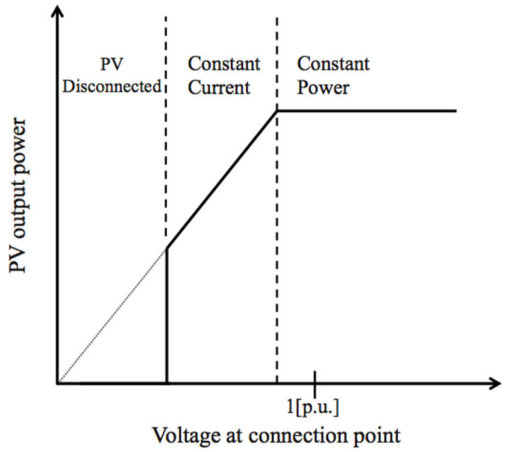

FIGURE 4. Relationship between PV voltage and its power output.

becomes more serious owing to the power imbalance, firstly. Nevertheless, the transient stability depends upon the amount of the disconnected PV capacity as well as the disconnecting speed of the PVs. Accordingly, it is significant to give the requirements on FRT and arm the PVs with the operation features of the PVs operating under the condition of the system fault to keep the power supply-require balance. Figure 5 represents Disconnecting features of the LVRT.

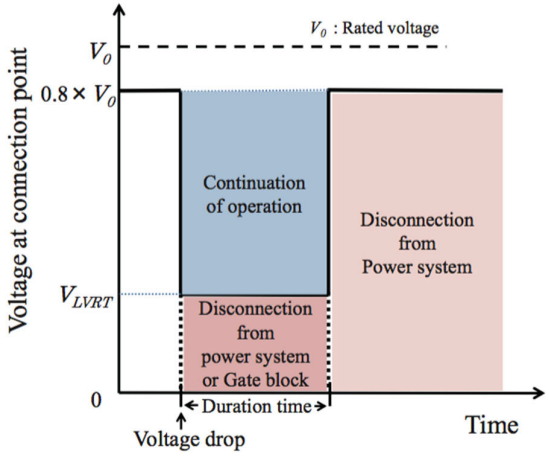

FIGURE 5. Disconnecting features of the LVRT.

The requirements for the PV's FRT include two aspects: the recovering features of the electrical power and the disconnecting characteristics of the PVs. Figure 5 above illustrates Disconnecting characteristics of the LVRT. The power system will disconnect from the PV fastly when the voltage of the connecting points drops under the threshold. In this article, the value is the so-called 'LVRT level' and uses '$\boldsymbol{V_{LVRT}}$' to symbolize it.

C. CONTROL PROCESS

The proposed algorithm connected the local transmitting system model in Figure 6 to every load node of the block transmission power system in Figure 7 below [37]. The connected nodes with the local transmitting model are 16, 18, 20, 22, and 23, respectively.

This paper Supposed a 3LG (Three-Line-to-Ground) fault as a disturbance in the trunk transmitting power system model (as shown in Figure 7).The 3LG error happens close to node 11 on that double-circuit transmitting line among nodes 11 and 12 at a time of 0.2 second.

The system will open that fault line at 0.36 second and reclose it when cleaning the fault. This situation is the most significant case in the power system of Figure 6.

D. CONSTANT IMPEDANCE LOAD

This article assumed two FRT requirements and assessed stabilities for every need. Tables 1 and 2 below give the cases in detail:

This article modeled the constant impedance load using the electric lighting load and the electrical load without the equipment with an inverter. The electricity consumption of each connection point drops as its voltage goes down. Figure 8 gives Rotor Angle with IM rate = 0[%] in the case of FRT 0.

NOTE PLEASE: the IM rate in all Figures below means a rate of active power devoured via the induction motor load to active power used at every node, and this rate is varied.

The system will open that fault line at 0.36 second and reclose it when cleaning the fault. This situation is the most significant case in the power system of Figure 8.

Figure 9 illustrates rotor angles in the case of FRT 1. As shown in this Figure, the more quickly the electrical power output of the PV recovers, the faster generators in the grid system accelerate.

Table 3 below illustrates the simulated results for two FRT requirements with an IM rate is no more than 40%. The symbol of '-' in this Table means the voltage instability due to the rotor angle instability. Table 3 shows that the more induction motors connected to the load node, the better the transient stability is.

Figure 10 gives Rotor Angle with an IM rate = 20[%] in the case of FRT 0. Compared to an IM rate = 0[%] in the case of FRT 0, a rotor angle with an IM rate = 20[%] can be stable soon to some extent.

Table 4 shows the proposed method is better than the traditional way.

Figure 11 illustrates rotor angles with IM rate = 20[%] in the case of FRT 1. As shown in this Figure, the more quickly the electrical power output of the PV recovers, the faster generators in the grid system accelerate. Furthermore, compared to instability when IM rate = 0[%] in the case of FRT 0, rotor angle with IM rate = 20[%] can be stable immediately.

In addition, Table 5 below depicts the simulation results of two FRT requirements with an IM rate is more than 40%. The mark of '–' in Table 4 has the same meaning as in Table 3, which is still the voltage instability due to the rotor angle instability. Table 5 indicates the more induction motors linked to the load points, the more unstable the voltage is.

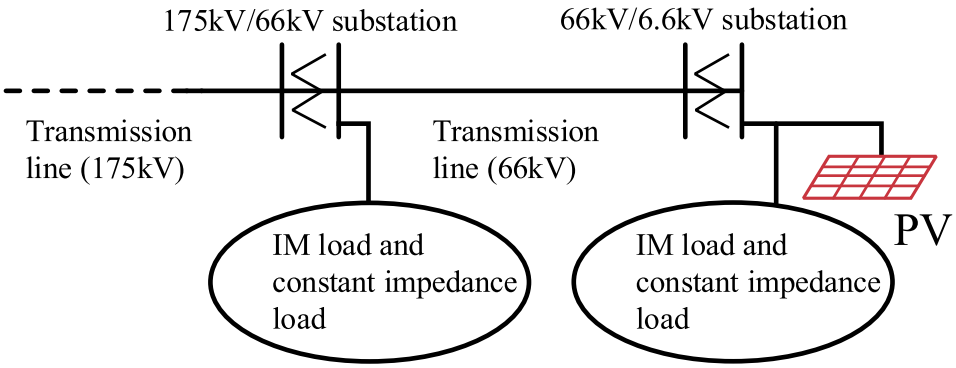

FIGURE 6. Local transmitting system model at every load node.

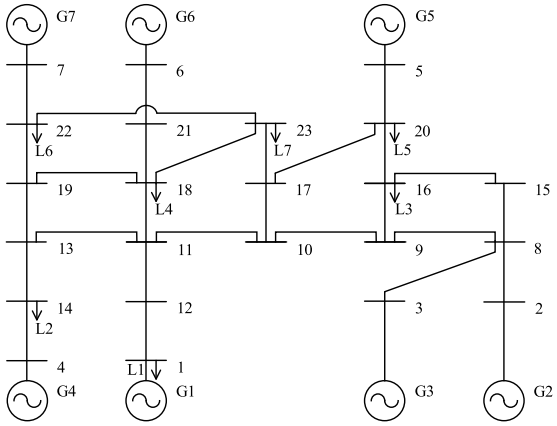

FIGURE 7. Trunk transmitting power system model.

Figures 12 and 13 give behaviors of the rotor angles with an IM rate = 50 % in the cases of FRT0 and FRT1. Figure 11 shows the rotor angle with an IM rate = 50[%] in the case of FRT 0 can not be stable immediately compared to the condition of an IM rate = 20[%].

Meanwhile, Figure 13 represents that the rotor angle with an IM rate = 50[%] in the case of FRT 1 also cannot be stable fastly compared to the condition of an IM rate = 20[%].

Consequently, Figures 7-12 show that the condition of a range from an IM rate = 20[%] to an IM rate=40[%] could best meet the requirements for the PV Outputting recovery.

E. INDUCTION MOTOR LOAD

The induction motor load is a characteristic of the dynamic load with a constant inputting power feature. The induction motor load's electrical consumption also decreases if the connection point's voltage drops due to the system fault.

Nevertheless, after that, it will recover via an increase of a slip of the inverter, which means, after that, it will recover by increasing the smoothness of the inverter, which means this induction motor load can approximately show a constant characteristic of the outputting power. Equations (12) and (13) represent the slip and the impedance of the induction motor load:

$$\frac{ds}{dt} = \frac{1}{M_{im}}\left(\frac{P_{mim}}{1-s} - P_{eim}\right) \tag{12}$$

$$Z'_{im} = \frac{\gamma_{im}}{s} + jX_{im} \tag{13}$$

In the expressions(12,13),M_{im} and s are the inertia and slip constant of the induction motor load; P_{eim} is Electrical power input; P_{mim} is Mechanical power output. γ_{im}, X_{im}, and Z'_{im} are resistance, inductance, and impedance of the induction motor load.

Figure 14 illustrates an instance of the recovering characteristics for the electrical power output. Once the voltage of

TABLE 1. FRT demands of disconnection.

Case	Level of LVRT		Demands of the PCS operation	
	Voltage [p.u.]	Duration time [s]	Voltage≥ LVRT level	Voltage<LVRT level
FRT 0	0.32	1.0	Keep working	Disconnected operation from grid system
FRT 1	0.21	1.1	Keep working	the gate block

TABLE 2. Requirements for the PV outputting recovery when the voltage recovers.

Case	Voltage≥LVRT level	Voltage<LVRT level
FRT0	recover more than 80% in 10 seconds	Disconnected from grid
FRT1	regain more than 80% in 0.5 seconds	egain more than 80% per second

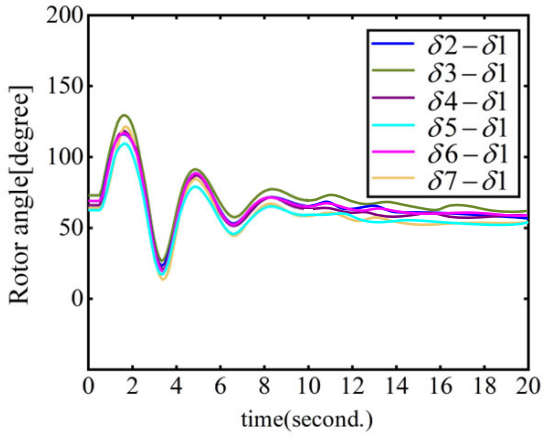

FIGURE 8. Rotor angle with IM rate = 0[%] in the case of FRT 0.

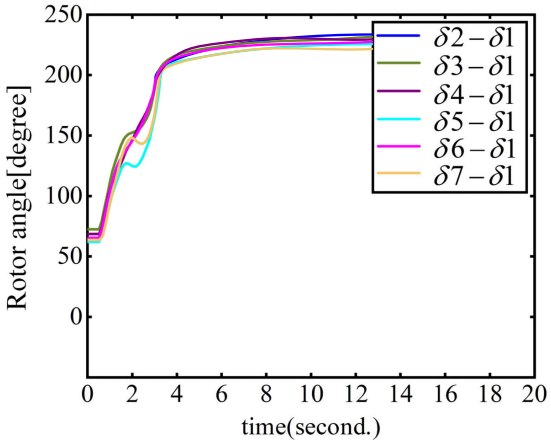

FIGURE 9. Rotor angle with IM rate = 0[%] in the case of FRT 1.

the connecting point drops but no less than the LVRT level because of a fault, the PV system can keep working and quickly regain its electrical power output to a fixed value of 80% of the rated level.

On the other hand, when the voltage is less than the level of the LVRT, using the gate block of the PCS disconnects the PV from the grid temporarily and reconnects to the grid system when the voltage recovers completely and restores its electrical power output to a given value. Otherwise, Figure 15 shows that voltages of the connecting points in PVs rapidly recover to more than 0.8[p.u.] from a sag when the system closes the circuit breaker over the error lines.

Furthermore, because the time of the generator's acceleration is nearly the same as the time of the recoveries for the electrical outputs, thus the rotor angle is unstable due to this recovery for the PV's electrical power output.

V. EXPERIMENTAL RESULTS AND RESULTS

A. EXPERIMENTAL RESULTS

As shown in Figure 16, this paper tested the proposed control scheme and the experiments completed for the single-phase smart inverter based on the QZSI technique.

TABLE 3. Assessment results of the stability (IM rate is no more than 40%) NOTE, please: the upper row indicates transient stability, and the lower row represents voltage stability in the Table.

	Type	IMrate [%]					
		0	2	10	20	30	40
FRT	0 Transien	√	√	√	√	√	√
	-t	√	√	√	√	√	√
	1 Voltage	×	√	√	√	√	√
		—	√	√	√	√	√

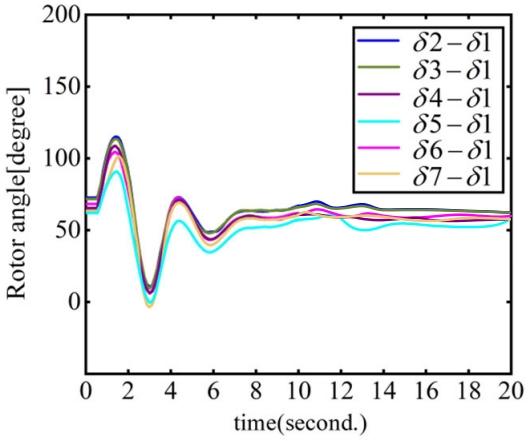

FIGURE 10. Rotor angle with IM rate = 20[%] in case FRT1.

TABLE 4. Assessment of the robustness.

Architecture	Technology	# FFs	# Slice	Freq (MHz)	Bit rate (Gbps)
Proposed method	GB100XCP12-227	641	786	266	9.09
Old MPC [10]	XC5VLX110T	-	575	232	7.1

TABLE 5. Assessment results of the stability (IM rate is more than 40%) NOTE, please: the upper row indicates transient stability, and the lower row represents voltage stability in the Table.

	Type	Index	IMrate [%]			
			40	45	50	55
FRT	0	Transient	√	—	—	—
			√	×	×	×
	1	Voltage	√	√	—	—
			√	√	×	×

In our experiments, the QZSI adopted GB100XCP12-227 SiC IGBT, the implementation practiced on dSPACE CP1103, and the sampling time is the 20s. This research

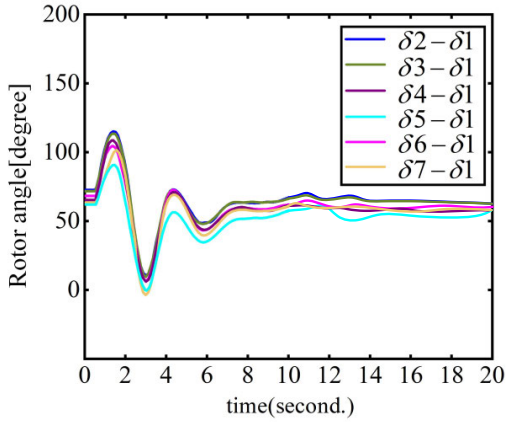

FIGURE 11. Rotor angle with IM rate = 20[%] in case FRT 1.

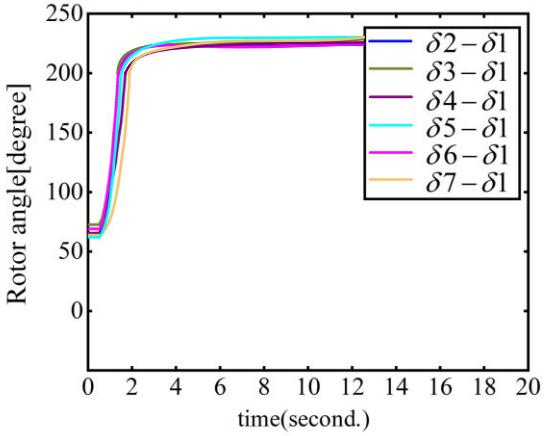

FIGURE 12. Rotor angle with IM rate = 20[%] in case of FRT 0.

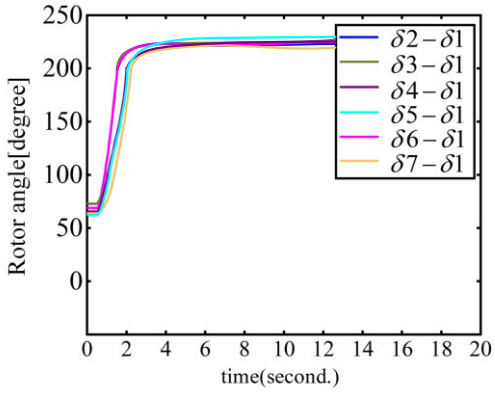

FIGURE 13. Rotor angle with IM rate = 20[%] in case FRT 1.

directly applied the gate signal from CP1103 to the QZSI gate driver from the digital CP1103 without the dead time. Although this direct operation is usually risky, the impedance network prevents unexpected current peaks during inadvertent traversal. In addition, the circuit can test grid voltage dips because of a connection between the output of the QZSI and

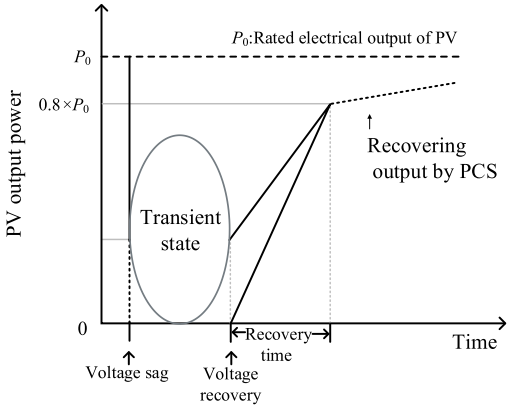

FIGURE 14. An instance of the recovering characteristics.

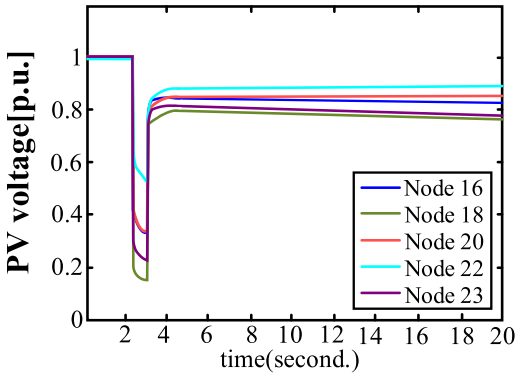

FIGURE 15. An instance of the recovering characteristics.

a bidirectional grid simulator. Furthermore, the power supply used to simulate 1 kW photovoltaic is EA-PSI 9000 2U and set its slope to 4 p.u., thus making RPI (Real Processing Index) display on an oscilloscope easier.

The experiments verified the performance of the proposed system by connecting the single-phase QZSI to the grid of the single-phase 120V RMS and 60 Hz. Table 4 illustrates the experimental parameters and their values:

Figures 17 and 18 give the dynamic characteristics during the grid voltage sag. As seen in Figure 16, the RMS grid voltage drops to 100 V from 120V at t1; i_{L1} symbolizes a change in the PV's power generation, and the fixed active power is 1000W.

Figure 17 shows that i_{L1} has no transient after t_1. Because the injection of the reactive power is easy to identify and the grid current lags behind the grid voltage, the pulse change of the i_{gref} leads to a sudden increase in the amplitude of the grid current. The power injection decreases briefly with the decrease of grid voltage and the constant amplitude of the active current. The initial reduction of power injection generates a surge at the DC port, and C1 stores excessive energy. Therefore, the PI controller starts to increase i_{dref}.

Figure 18 shows the voltage in the complete DC port for the extended interval. The DC port voltage reaches a steady state with the increase of the i_{dref}. This setting time depends

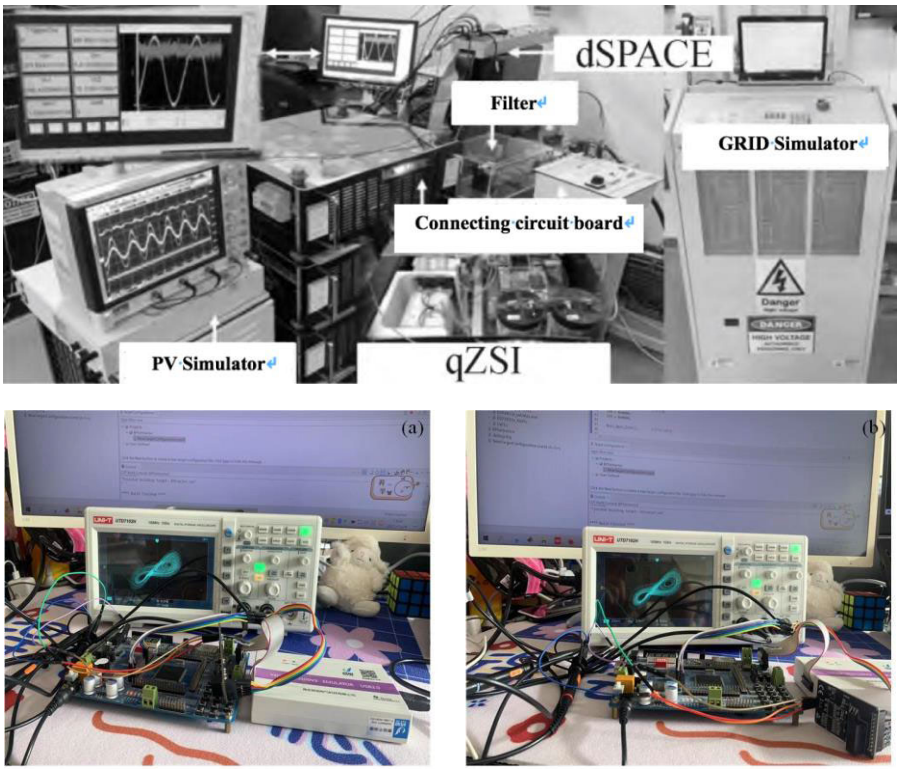

FIGURE 16. Hardware archetype of the single-phase grid connection QZSI.

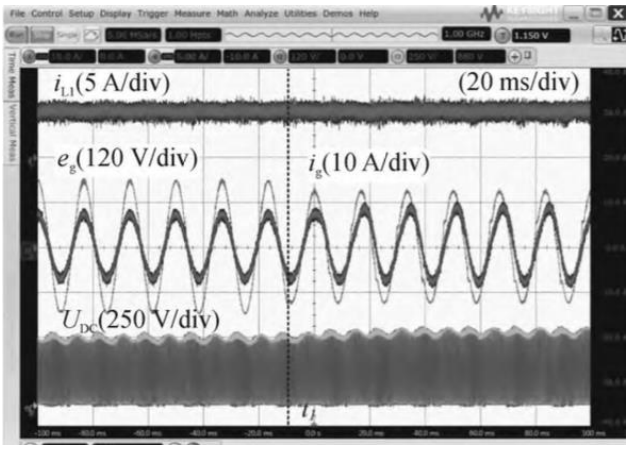

FIGURE 17. Dynamic response of grid voltage and current, inductance L current and DC link voltage.

on the gain of the PI controller. Consequently, increasing the sampling frequency of the PI or improving the integral receiving can shorten the stability time of the voltage of the DC port.

B. SIMULATION FOR THE TRACKING PERFORMANCE OF THE SYSTEM

Figure 19 depicts the autonomous tuning performance of the proposed algorithm in this paper. As shown in this Figure that the presented algorithm in the article can stabilize the grid outputting voltage in a short time (approximately 0.6 second) when the grid fails (i.e., voltage dipping).In addition, once the grid voltage recovers to the natural state, the increased active current injection draws the extra energy from the capacitor C1, which leads to the voltage sag. Furthermore, the grid voltage can become normal when the PI controller reaches U_{C1}.

The reason is that increasing the sensitivity of the PI controller will generate a large number of steady-state oscillations on the i_{dref} and increase the sub-harmonic distortion of the injected current. These oscillations are the result of voltage fluctuations on C1. Considering that the actual efficiency of the power level is somewhat different between the photovoltaic reference power and the real power injected into the grid, the authors will select the power benchmark using a flexible MPPT algorithm to address the low-efficiency problem in our future research.

Observing the transient performance of the control scheme (i.e., the stability time under the instant conditions) and other indicators can reveal the tracking performance of the system because the transient performance is highly dependent on the reference value but only the input of predictive control. To test the tracking performance of the proposed method, the tracking error defined in this paper is:

$$x_\varepsilon[k] = \left|x^*[k-1] - x[k]\right|, x \in \left[i_{L1}, i_g\right] \tag{14}$$

The target tracking error is undoubtedly the most appropriate measurement because this value indicates the extent to which the controlled variable reaches its reference value in

TABLE 6. Experimental parameters.

Parameters	Values	Parameters	Values
Grid frequency/Hz	65	ε	1 $\times 10^{-4}$
Sampling frequency in MPC/kHz	55	(U_{MPP}/U_{OC})/V	205/238
Sampling frequency in MPPT/kHz	6.25	(I_{MPP}/I_{SC})/A	4.9/5.5
Sampling frequency in PI (Proportional integral)/kHz	3.235	$(L_1/L_2)/\mu H$	0.4
Gain in PI controller	0.007/0.078	(C_1/C_2)/mF	1.5
size of the RMS window	834	$C_{PV}/\ \mu H$	210
the weight factor of the window	100	C_f/mF	2.6
$R_{/\!/}$/mΩ	200	γ/p.u.	5
Grid Voltage/V	125	U_{C1}^{*}/V	280

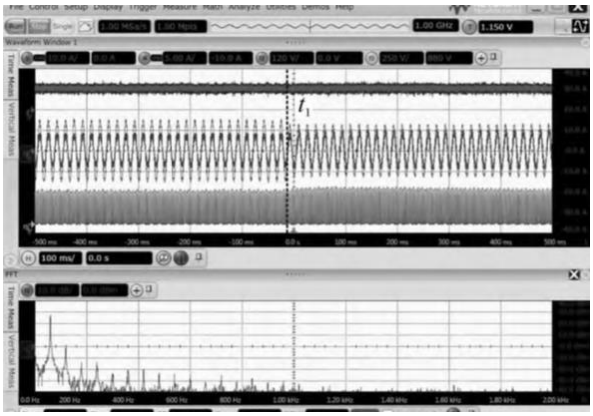

FIGURE 18. A dynamic diagram of DC port voltage and an FFT diagram of injected grid current.

the next sampling period. This paper gives the tracking error difference in the control scheme to show the tracking error at each control point. Figure 20 below illustrates the tracking performance of the system. Also, this Figure gives a ratio

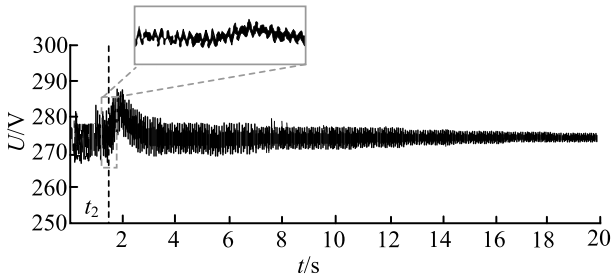

FIGURE 19. A Diagram of voltage sag applying the constant average active power strategy.

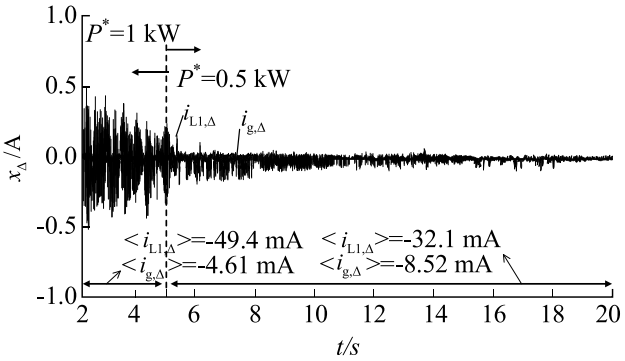

FIGURE 20. Tracking performance of the system.

tracking error comparison between the auto-tuned weight coefficient and the fixed factor. For clarity, this report defines the measurement in Figure 13:

$$x_{\Delta}[k] = x_{\varepsilon,\text{auto}}[k] - x_{\varepsilon,\text{fixed}}[k], \quad x \in \left[i_{\text{L1}}, i_{\text{g}}\right] \tag{15}$$

In equation (15), $x_{\varepsilon,\text{auto}}$ and $x_{\varepsilon,\text{fixed}}$ are the tracking error of the proposed control and the fixed weight coefficient ratio control. Therefore, negative x_{Δ} means better tracking through the proposed autonomous tuning control.

As shown in Figure 20, x_{Δ} symbolizes the step change from 1 kW to 0.5 kW for flexible power-point reference value tracking under normal conditions and whole solar irradiance occurring at t_6. Simulation results prove that simulation and experimental results showed that the condition of a range from an IM rate = 20[%] to an IM rate = 40[%] could best meet the requirements for the PV outputting recovery.

Figures illustrate that by making the reduction of PV power proportional to the decrease in grid voltage, the active reference current remains unchanged under a steady state. However, the reactive current reference will still increase the grid current amplitude. MPC reduces the input current by avoiding the penetration state. Putting the steady-state values of U_{PV} and U_{C1} into the equation in the paper, which is the penetration produces positive d_{iL1}/dt, while the non-penetration state is the opposite.

Although the magnitude of i_{L1} is more than i_g, the average values of both sides are negative. The results show that

the overall tracking effect of the two targets is better with the proposed control, and the difference between the two values decreases slightly after t_6. Because the amplitude of the two control targets reduced and the photovoltaic power also decreased, that is, the average tracking error of the input current reduced by nearly 10%, and the average output current tracking error reduced by about 4%, which shows that the tracking performance has significantly improved.

VI. CONCLUSION

Firstly, this paper assessed the voltage stability and transient stability of a power system with one multi-machine connected to an immense amount of the PV generations. Nevertheless, the voltage can not be stable if there are too many induction motors in the power system, so the quick reconnection of the PV generations behind those faults can better the voltage stability.

Nevertheless, if the power system connected to too many induction motors, then the voltage is going to not be stable, but the quick reconnection of the PV generations behind those faults can better the voltage stability.

Furthermore, this paper proposed the autonomous model predictive control (AMPC) scheme for intelligent PV inverters to achieve smooth switching between LVRT and MPPT modes under random grid conditions.

Finally, the simulation and experimental results verified the system performance of the reactive power injection strategy in LVRT mode, and the injected reactive power conforms to the latest grid specifications. Both simulation and experimental results showed that the condition of a range from an IM rate = 20[%] to an IM rate = 40[%] could best meet the requirements for the PV outputting recovery and the average tracking error of the input current reduced by nearly 10%. Also, the average output current tracking error reduced by about 4%, which shows that the tracking performance has significantly improved.

Because there is a difference between the photovoltaic reference power and the actual power injected into the grid, the authors will select the power benchmark of the flexible power point tracking algorithm to deal with the low efficiency in the power conversion stage in our future research.

AUTHOR CONTRIBUTIONS

Wang Jinpeng designed the measurement scheme, carried out the simulations, and wrote the paper; Zhao Xin supervised the work, arranged the architecture, and contributed to the writing of the paper; and Zhang Bo, Yao Qinxue, and Jeremy-Gillbanks performed the field test and analyzed the data.

CONFLICTS OF INTEREST

The authors declare no conflict of interest.

REFERENCES

[1] W. Jinpeng, Z. Yang, G. Xin, and J.-G. A. Z. Xin, "A hybrid predicting model for the daily photovoltaic output based on fuzzy clustering of meteorological data and joint algorithm of GAPS and RBF neural network," *IEEE ACCESS*, vol. 10, pp. 30005–30017, 2022.

[2] Z. Zheng, W. Song, and H. Lin, "A stabilization control for PMSM drive system equipped with reduced DC-link capacitor," in *Proc. IEEE CIEEC*, Sep. 2019, pp. 1518–1523.

[3] X. Liang, "Emerging power quality challenges due to integration of renewable energy sources," *IEEE Trans. Ind. Appl.*, vol. 53, no. 2, pp. 855–866, Mar./Apr. 2017.

[4] A. Sangwongwanich, Y. Yang, F. Blaabjerg, and H. Wang, "Benchmarking of constant power generation strategies for single-phase grid-connected photovoltaic systems," *IEEE Trans. Ind. Appl.*, vol. 54, no. 1, pp. 447–457, Jan./Feb. 2018.

[5] G. Wang, R. Liu, N. Zhao, D. Ding, and D. Xu, "Enhanced linear ADRC strategy for HF pulse voltage signal injection-based sensorless IPMSM drives," *IEEE Trans. Power Electron.*, vol. 34, no. 1, pp. 514–525, Jan. 2019.

[6] S. S. Badini and V. Verma, "A new stator resistance estimation technique for vector-controlled PMSM drive," *IEEE Trans. Ind. Appl.*, vol. 56, no. 6, pp. 6536–6545, Nov. 2020.

[7] A. K. Panchal, "A per-unit-single-diode-model parameter extraction algorithm: A high-quality solution without reduced-dimensions search," *Sol. Energy*, vol. 207, pp. 1070–1077, Sep. 2020.

[8] H. A. Khawaldeh, H. Aljarajreh, M. Al-Soeidat, D. D.-C. Lu, and L. Li, "Performance investigation of a PV emulator using current source and diode string," in *Proc. 26th Int. Conf. Syst. Eng. (ICSEng)*, Dec. 2018, pp. 1–5.

[9] G. Zemeng, W. Li, and H. Yang, "MMC DC bipolar short-circuit lock—Free fault crossing control strategy for distribution network," *High Voltage App.*, vol. 56, no. 6, pp. 274–281, 2020.

[10] S. Mukherjee, V. R. Chowdhury, P. Shamsi, and M. Ferdowsi, "Power-angle synchronization for grid-connected converter with fault ride-through capability for low-voltage grids," *IEEE Trans. Energy Convers.*, vol. 33, no. 3, pp. 970–979, Sep. 2018.

[11] M. Dietmannsberger, F. Grumm, and D. Schulz, "Simultaneous implementation of LVRT capability and anti-islanding detection in three-phase inverters connected to low-voltage grids," *IEEE Trans. Energy Convers.*, vol. 32, no. 2, pp. 505–515, Jun. 2017.

[12] P. R. Bharathi, R. Mahendran, S. Priya, and A. Suresh, "Hybrid pulse width modulated three-phase quasi-Z-source grid-tie photovoltaic power system," *Int. J. Eng. Res.*, vol. 7, no. 2, Feb. 2018.

[13] S. B. Kjaer, J. K. Pedersen, and F. Blaabjerg, "A review of single-phase grid-connected inverters for photovoltaic modules," *IEEE Trans. Ind. Appl.*, vol. 41, no. 5, pp. 1292–1306, Sep./Oct. 2005.

[14] D. Bao, X. Pan, Y. Wang, H. Huang, and B. Wu, "Integrated-power-control-strategy-based electrolytic capacitor-less back-to-back converter for variable frequency speed control system," *IEEE Trans. Ind. Electron.*, vol. 67, no. 12, pp. 10065–10074, Dec. 2020.

[15] X. Huang, X. Ruan, J. Fang, and S. Kan, "A virtual impedance based control scheme for modular electrolytic capacitor-less second harmonic current compensator," *IEEE Trans. Ind. Electron.*, vol. 68, no. 1, pp. 198–209, Jan. 2021.

[16] T. Shinagawa, K. Ohishi, K. Abe, Y. Yokokura, and T. Inoue, "Harmonics reduction control of source current of electrolytic capacitorless inverter for position-sensorless drive system of induction motors," in *Proc. 23rd Int. Conf. Electr. Mach. Syst. (ICEMS)*, Nov. 2020, pp. 928–933.

[17] K. Abe, H. Haga, K. Ohishi, and Y. Yokokura, "Direct DC-link current control considering voltage saturation for realization of sinusoidal source current waveform without passive components for IPMSM drives," *IEEE Trans. Ind. Electron.*, vol. 65, no. 5, pp. 3805–3814, May 2018.

[18] D. Wang, K. Lu, P. O. Rasmussen, L. Mathe, Y. Feng, and F. Blaabjerg, "Voltage modulation using virtual positive impedance concept for active damping of small DC-link drive system," *IEEE Trans. Power Electron.*, vol. 33, no. 12, pp. 10611–10621, Dec. 2018.

[19] Y. Huang, M. Shen, F. Z. Peng, and J. Wang, "Z-source inverter for residential photovoltaic systems," *IEEE Trans. Power Electron.*, vol. 21, no. 6, pp. 1776–1782, Nov. 2006.

[20] D. Jun, Z. Minghang, and L. Kunxiong, "Local voltage selective control strategy based on power regulation of photo-voltaic grid-connected inverter," *Power Capacitor Reactive Power Compensation*, vol. 40, no. 1, pp. 148–153, 2019.

[21] Y. Liu, H. Abu-Rub, and B. Ge, "Z-source/quasi-Z-source inverters: Derived networks, modulations, controls, and emerging applications to photovoltaic conversion," *IEEE Ind. Electron. Mag.*, vol. 8, no. 4, pp. 32–44, Dec. 2014.

[22] J. Anderson and F. Z. Peng, "Four quasi-Z-source inverters," in *Proc. IEEE Power Electron. Spec. Conf.*, Jun. 2018, pp. 2743–2749.
[23] Y. Liu, *Impedance Source Power Electronic Converters*. Hoboken, NJ, USA: Wiley, 2020.
[24] H. A. Khawaldeh, M. Al-Soeidat, D. D. Lu, and L. Li, "Simple and fast dynamic photovoltaic emulator based on a physical equivalent PV-cell model," *J. Eng.*, vol. 2021, no. 5, pp. 276–285, May 2021.
[25] N. Ullah, F. Nisar, and A. A. Alahmadi, "Closed loop control of photo voltaic emulator using fractional calculus," *IEEE Access*, vol. 8, pp. 28880–28887, 2020.
[26] D. Ding, G. Wang, N. Zhao, G. Zhang, and D. Xu, "Enhanced flux-weakening control method for reduced DC-link capacitance IPMSM drives," *IEEE Trans. Power Electron.*, vol. 34, no. 8, pp. 7788–7799, Aug. 2019.
[27] W. Zhang and J. W. Kimball, "DC–DC converter based photovoltaic simulator with a double current mode controller," *IEEE Trans. Power Electron.*, vol. 33, no. 7, pp. 5860–5868, Jul. 2018.
[28] J.-E. Hernandez-Diez, C.-F. Mendez-Barrios, S.-I. Niculescu, and E. Barcenas-Barcenas, "A current sensorless delay-based control scheme for MPPT-boost converters in photovoltaic systems," *IEEE Access*, vol. 8, pp. 174449–174462, 2020.
[29] D. Ding, G. Wang, N. Zhao, G. Zhang, and D. Xu, "An antiovervoltage control scheme for electrolytic capacitorless IPMSM drives based on stator current vector orientation," *IEEE Trans. Ind. Electron.*, vol. 67, no. 5, pp. 3517–3527, May 2020.
[30] P. Xingyu, G. Deshu, and K. Qingpai, "Power capacitors and reactive power compensation," vol. 40, no. 4, pp. 183–187, 2019.
[31] S. Vazquez, J. Rodriguez, M. Rivera, L. G. Franquelo, and M. Norambuena, "Model predictive control for power converters and drives: Advances and trends," *IEEE Trans. Ind. Electron.*, vol. 64, no. 2, pp. 935–947, Feb. 2017.
[32] M. Farahani, M. A. Shamsi-nejad, and H. R. Najafi, "Design and construction of a digital solar array simulator with fast dynamics and high performance," *Sol. Energy*, vol. 196, pp. 319–326, Jan. 2020.
[33] S. E. I. Remache, A. Y. Cherif, and K. Barra, "Optimal cascaded predictive control for photovoltaic systems: Application based on predictive emulator," *IET Renew. Power Gener.*, vol. 13, no. 15, pp. 2740–2751, Nov. 2019.
[34] Z. Qian, W. Yao, and K. Lee, "Dynamic DC-link over-voltage mitigation method in electrolytic capacitor-less adjustable speed drive systems," in *Proc. IEEE Energy Convers. Congr. Expo. (ECCE)*, Sep. 2018, pp. 4628–4632.
[35] L. J. Jeremy, C. A. Ooi, and J. Teh, "Non-isolated conventional DC–DC converter comparison for a photovoltaic system: A review," *J. Renew. Sustain. Energy*, vol. 12, no. 1, Jan. 2020, Art. no. 013502.
[36] L. Mathe, L. Torok, D. Wang, and D. Sera, "Resonance reduction for AC drives with small capacitance in the DC link," *IEEE Trans. Ind. Appl.*, vol. 53, no. 4, pp. 3814–3820, Jul. 2017.
[37] R. Ayop and C. W. Tan, "Rapid prototyping of photovoltaic emulator using buck converter based on fast convergence resistance feedback method," *IEEE Trans. Power Electron.*, vol. 34, no. 9, pp. 8715–8723, Sep. 2019.

WANG JINPENG was born in Wulanhaote, Xingan, China, in 1979. His current research interest includes numerical optimization.

ZHANG BO received the B.S. degree in electronic engineering from the Harbin University of Technology, Heilongjiang, China, in 2001. He is currently pursuing the master's degree with Dalian Polytechnic University, Dalian, China.

YAO QINXUE received the B.S. and M.S. degrees in electronic engineering from the University of Zhengzhou, Henan, in 2019. He is currently pursuing the master's degree with Dalian Polytechnic University, Dalian, Liaoning, China.

JEREMY-GILLBANKS was born in Perth, Western Australia, Australia, in 1977. He is currently pursuing the Ph.D. degree with The University of Western Australia, Australia. He has authored and coauthored several research articles indexed in either Scopus or Web of Science.

ZHAO XIN (Member, IEEE) was born in Jinzhou, Liaoning, China, in 1968. He is currently a Professor with Dalian Polytechnic University. His current research interest includes numerical optimization.